*International Journal of Research in Engineering and Science (IJRES)*
*ISSN (Online): 2320-9364, ISSN (Print): 2320-9356*
*www.ijres.org Volume 13 Issue 6 ǁ June 2025 ǁ PP. 74-88*

# Detection of surface and subsurface flaws with miniature GMR-based probe

Ngoc-Ha Nguyen, Thang Nguyen Huu

***Abstract—****The small feature size and high sensitivity of the giant magnetoresistance (GMR) sensors make them suitable for applications in the magnetic-field-based imaging requiring high spatial resolution and detection. In this work, we proposed a novel design of the absolute miniature eddy-current probe with a spin-valve GMR sensor chip. The sensor chip is excited by the alternating magnetic field induced by a tiny coil with a feature size of 3 mm. In the absolute probe, the in-house-made GMR sensor is in a half-bridge configuration comprising two cascaded elements in parallel with an external variable resistor. The two active elements on the chip are excited by a tiny coil aligned to the position that balances the output of the bridge. In this way, two elements effectively form an axial gradiometer with the bottom GMR element sensitive to the surface defect on a conductive specimen. The performance of the absolute probe is verified by scanning it on the simulated defects on the metallic sample. With this design, the achieved spatial resolution is better than 2 mm. The proposed device is useful in the detection of surface and sub-surface defects on the metallic material, such as cracks, metal loss, and miscellaneous mechanical damages.*

***Index Terms—*** *Nondestructive testing, Eddy current, Giant magnetoresistance, Defect detection*

---

Date of Submission: 24-05-2025 Date of acceptance: 04-06-2025

---

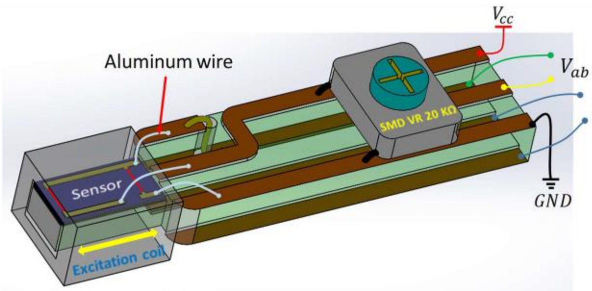


## I. Introduction

IN recent decades, the need for controlling the product quality and testing the structural integrity of the conductive materials is essential in the production and use process where non-destructive testing (NDT) techniques based on the eddy-current (EC) effect is widely applied. The advantage of these eddy-current effect-based methods is that it allows position and shape determination, and size estimation of defects on the conductive materials and does not require any contact between the tested specimen and the probe. even if defects are deeply buried in the material structure are not detected by external inspection. Several techniques including analytical, numerical, and experimental solutions have been developed to determine the characteristics of the defect on the conductive sample such as calculation of the depth and opening of a long crack [1], the analytic model of an ideal surface crack [2], or the impedance analysis of the coils for testing the surface crack based on the finite-element and boundary element models [3],[4]. For experimental methods, the structural integrity is evaluated by using an excitation coil and a field sensor, consisting of metal crack detection using Hall sensors [5] and superconducting quantum interference device (SQUID) [6],[7], in which the usage of the giant-magnetoresistance (GMR) sensors with high sensitivity, low-cost, and wide frequency range is increasingly playing an important role in many fields, including non-destructive testing in industries [8]-[9], cancer cell detection in medicine [10], and electronic compasses in consumer electronics [11]. The most prominent applications of GMR sensors include the detection of tiny magnetic objects as well as imaging of defects on the conductive sample surface to characterize the shape, size, and depth of flaws and cracks. The rapid estimation of crack geometry and corrosion detection is demonstrated by using the eddy-current probe with the on-chip [8],[12],[13],[14] or packaged GMR sensor arrays

Manuscript received M 13. Corresponding author: Thang Nguyen Huu (e-mail: Nguyenhuuthang@tnut.edu.vn).
Ngoc-Ha Nguyen, Thang Nguyen Huu, are The faculty of Mechanical Engineering, Thai Nguyen University of Technology, Thai Nguyen 250000, Vietnam.

[9]. However, the linear arrangement of the array makes it applicable only to the sample with a flat surface. Furthermore, reducing the spacing between array elements does not improve the spatial resolution a lot since the ultimate limit is set by the relatively large sensor-to-sample distance. Therefore, it is not suitable for applications requiring high sensitivity and accuracy on a flat or curved metal surface. The reliability and capability of the probe based on a single GMR sensor combined with different excitation coils [15]-[19] for defect detection have been also reported. For detecting deep seated cracks more than 5.0 mm, the probe with combination of a ferrite core excitation coil of a 10-mm outer diameter and a packaged GMR sensor fixed next the excitation coil is used [15]. However, the spatial resolution is limited due to increasing the horizontal size (which is equal to the total of the coil and GMR dimensions) and the maximum sensitivity for the $B_z$ component of the secondary magnetic field can not achieve in this design. For two-dimension defect detection, the image resolution can be improved based on the usage of a long meander coil [16] or a planar coil [17] serving as an excitation coil, but the probe with these big excitation coils is not suitable for the applications having the small scanning space. It is also reported that a short, minor surface crack of 2-mm length, 0.5-mm width, and 1.0-mm depth is reliably detected by the EC probe including the flat spiral coil of 5.6-mm diameter and a packaged GMR [18], but for the shorter crack of 1 mm, the crack is not clearly observed due to decrease in peak amplitude values of the crack, approaching the system noise. However, it is proposed that the further reduction in the coil diameter is a potential method to clearly detect shorter cracks. The disadvantage of these designs is the limitation of the spatial resolution which requires the small sensing space of the probe and the maximum sensitivity can not achieve due to the unsuitable coil-sensor arrangement, the sensor used in the package configuration, and the minimum lift-off limitation including the thickness of the excitation coil. Besides, the usage of the big excitation coil in inspecting small defects is limited due to the enhancement of the penetrating depth and probed volume which result in a further decrease of the output amplitude in the overall sensitivity of the test [20].

In our work, a different approach with the proposed design aims at enhancing the spatial resolution for detecting the minor, short surface and subsurface defects, such as fatigue cracks, inclusions, voids, and corrosion for the conductive material or shorts in a printed circuit. Currently, to satisfy the high spatial resolution requirement and small defect detection, the coil-based probe with the small diameter is proposed [21],[22]. However, the sensitivity is reduced due to the induced voltage depended proportionally on the magnetic flux through the pickup coil's cross-section area [23], therefore the sensor based on the small coil diameter is limited and can not achieve the high-performance requirements and it is only suitable for applications of the high excitation frequencies. It is necessary to propose a novel design of the EC probe with a specialized GMR sensor for detecting the minor flaws so that the obtained EC signals can clearly extract the features of the flaw. In this work, a miniature EC probe based on the in-house made GMR in a half-bridge configuration and a tiny rectangular exciting coil is proposed and fabricated. The opening of the tiny rectangular exciting coil with a total size of less than 3.1 mm fits well to the shape of the half-bridge GMR. With the optimal chip-coil arrangement, the lift-off distance from the sensor/coil to the tested sample is significantly minimized and the spatial resolution is achieved to enhance the EC signals in NDT applications. The proposed probe is simple and compact in construction because no auxiliary coil or circuit is needed to compensate for the interference induced by excitation. The results with the performance of the proposed probe are analyzed and discussed.

## II. EXPERIMENT SETUP

### A. *Design of eddy current probe with a spin-value GMR sensor*

There are several implementations of the spin-valve GMR

TABLE I
Geometric properties of the excitation coil

| Quantity | Dimensions |
|---|---|
| Inside dimensions | 1.6 × 1.8 mm |
| Outside dimensions | 2.9 × 3.1 mm |
| Height coil | 1.42 mm |
| Diameter of wire | 0.05 mm |
| Lift-off $l_0$ | 0.2 mm |
| Number of turn | 252 |

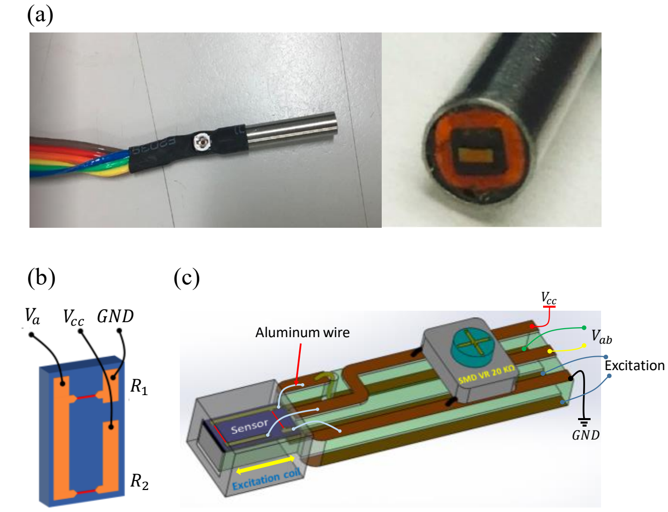


Fig. 1. The absolute eddy-current probe with a half-bridge GMR sensor chip. (a) Photographs of the encapsulated probe. (b) The structure of the half-bridge GMR sensor chip. (c) The structure of the probe.

sensor fabricated on a single chip. With the unidirectional pinned field, the most feasible designs are the half- and full-bridge layouts with two active GMR elements. The latter one is the typical design of the commercially available GMR chip, GF708 of Sensitec GmbH, which comprises two passive GMR elements covered by magnetic shielding films as the reference. In the current work, we proposed the design for a kind of miniature eddy-current probe, the absolute probe, comprising a half-bridge GMR chip, as shown in Figs 1. In the absolute probe, an in-house made half-bridge GMR sensor is used and this GMR sensor consists of a GMR chip, a tiny printed circuit board, an SMD variable resistance 20 kΩ, an excitation coil, and a stainless-steel packing tube. The specifications of the miniature excitation coil in the eddy current probe are shown in Table. 1. and the excitation frequency is designed above 1 MHz. In order to operate the sensor at the working point with the best sensitivity, the DC bias and AC excitation fields are generated by the same excitation coil at the same time. The coil must be fixed at the position where the sensing and reference element receives the same excitation intensity to balance the output, as shown in Fig. 1. The excitation coil is driven by the sinusoidal voltage with the peak-to-peak voltage $V_{pp}$ = 4.3 V at various frequencies to generated the excitation field. The half-bridge sensor is fabricated on a chip with two active GMR elements. One is the reference element $R_1$ and the other is the sensing element $R_2$, as shown in Fig. 1(b). The distance between the two sensing elements is about 1.5 mm. Each of the GMR elements is 5 μm in width with the zero-field resistance of about 3.2 kΩ for the

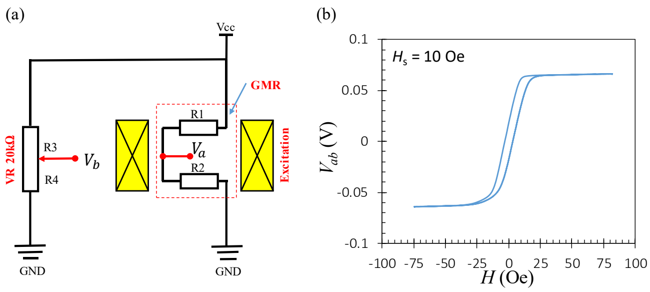


Fig. 2. The characteristics of the proposed probe: (a) Circuit diagram of the absolute eddy-current probe consisting of the half-bridge GMR sensor chip and SMD VR 20 kΩ. (b) The V-H curve of the probe.

sensing element and 2.83 kΩ for the reference element. Although both the upper reference element $R_1$ and the lower sensing element $R_2$ can detect the eddy-current magnetic field, the output of the half-bridge depends mainly on the change in $R_2$ when the object under test is close to the eddy-current probe. The change in $R_2$ is more significant since the reference element $R_1$ is more than 1 mm farther from the object under test.

To form the absolute eddy-current probe, the half-bridge GMR chip is attached to a tiny printed-circuit board (PCB) with the sensing direction parallel to the length dimension of the PCB. The aluminum wire bonding method is used to electrically connect the GMR chip to the PCB. A 20-kΩ SMD variable resistance is connected in parallel to the GMR chip to balance the output of the eddy-current probe, as shown in Fig. 2(a). With this way, the sensing axis of the GMR sensor is perpendicular to the specimen surface. It means that only the $B_z$ vertical component of the secondary magnetic field is sensed by the probe and it has very high in-plane magnetic sensitivity and extremely low hysteresis, which helps simplifying the mechanical design of the eddy-current probe. The 3.0-V DC supply voltage ($V_{cc}$) is provided by a battery set. The output voltage of the sensor is the difference between the field-dependent half-bridge voltage $V_a$ and the passive potential $V_b$ of the variable resistance, where

$$V_{ab} = V_a - V_b = V_{cc} \times \left( \frac{R_2(H)}{R_1(H) + R_2(H)} - \frac{R_4}{R_3 + R_4} \right) (1)$$

The output characteristic of the proposed probe was measured by a sinusoidal excitation magnetic field (Helmholtz Coil) at the excitation frequency of 1 kHz and the probe was fixed in a uniform reference magnetic field so that the direction of the pinning field on the GMR sensor is parallel with the direction of the reference magnetic field.

TABLE II
GEOMETRICAL CHARACTERISTIC OF MACHINED HOLES ON PCB

| Defects number | $D_1$ (mm) | $D_2$ (mm) | $D_3$ (mm) |
|---|---|---|---|
| $F_1$ | *0.75* | 1.75 | 4.75 |
| $F_2$ | *1.5* | 3.5 | 6.5 |
| $F_3$ | *2.0* | 4.5 | 7.5 |
| $F_4$ | *3.5* | 5.5 | 8.5 |

The voltage-field (V-H) curve of the proposed probe is shown in Fig. 2(b). It is seen that the voltage versus magnetic field curve is nonlinear and asymmetric to the zero magnetic fields and the sensor is saturated when applied magnetic field is greater than 10 Oe. However, in a small measurement arrange, from -7.5 to 7.5 Oe, the V-H response of the probe can be estimated linearly because the measured magnetic field in EC inspection is usually much less than 7.5 Oe. In the linear range, the sensitivity of half-bridge GMR based eddy-current probe was found to be 18 (mV/V)/mT.

### B. *Kinds of the specimen under test*

To verify performance of the designed probe, the nondestructive inspection is considered on two types of samples. The first sample is the aluminum plate of 90 x 50 x 5 mm in dimensions for surface and sub-surface defects detection. Designed cracks which are numbered 1–6 on specimen have the same length (50 mm) and width (0.5 mm), while the depth is respectively changed by 0.1, 0.3, 0.5, 1.0, 1.5, and 1.8 mm, as shown in Fig. 4(b). The distance between the crack centers is 14.3 mm. For surface defect inspection ( $h$ = 0 mm), the probe is placed on the specimen surface. For sub-surface flaws, the aluminum plate with machined cracks is attached by one aluminum tape layer and three aluminum tape layers as shown in Fig. 4(c) and (d), respectively. Each aluminum tape layer consists of an adhesive layer of 0.03 mm and a thin aluminum layer of 0.065 mm. Therefore, the machined cracks on the aluminum sample are buried at positions of $h$ = 0.095 and 0.285 mm under the top surface corresponding to one and three aluminum tape layers attached.

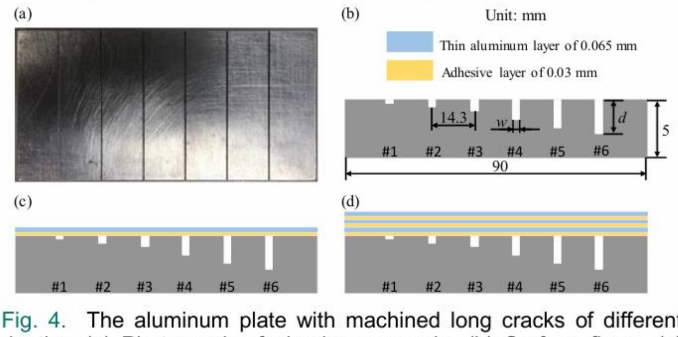


Fig. 4. The aluminum plate with machined long cracks of different depths. (a) Photograph of aluminum sample. (b) Surface flaws. (c) Subsurface flaws below an aluminum tape layer. (d) Subsurface flaws below three aluminum tape layers.

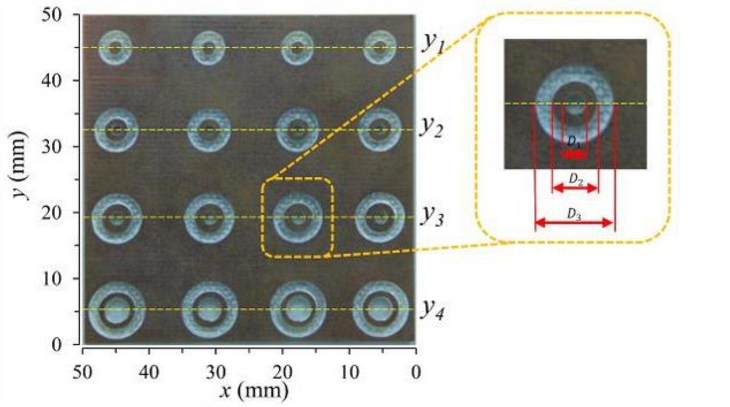


Fig. 5. Photograph of test specimen and geometrical dimensions of machined flaw on printed circuit board.

The second type of sample is a square-printed circuit board (PCB) of 50 x 50 mm in dimensions with the metal loss which is made by an engraving machine. The shape of the machined flaws is depicted in Fig. 5 and geometrical dimensions of flaws on PCB are in Table II. Each artificial flaw is expressed by a inside circle hole having diameter of $D_1$ and a scarf shape which is limited by diameters of $D_2$ and $D_3$, as described in Fig. 5. There are four kinds of flaw with different dimensions of $D_1$, $D_2$ and $D_3$ which are marked $F_1$–$F_4$ where four flaws $F_1$, four flaws $F_2$, four flaws $F_3$ and four flaws $F_4$ are located on lines $y_1$, $y_2$, $y_3$, and $y_4$, respectively. The extension of geometrical dimensions of machined slots and holes is necessary to demonstrate high spatial resolution flaw detector of the GMR probe, which require the variety of sizes and profiles of defects.

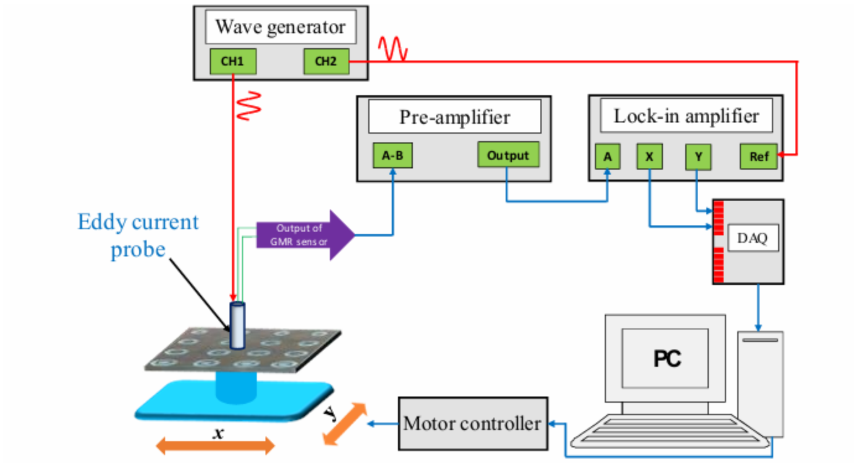


Fig. 6. The block diagram of the automatic system for detecting flaw based on half-bridge GRM sensor.

### C. *Experimental eddy-current flaw detection system*

In the GMR eddy-current system, the excitation field is induced by injecting a sine wave-current signal into the excitation coil surrounding the GMR sensor. The amplitude of the excitation signal for the proposed probe can change from 1 V to 10 V in peak-to-peak value with various frequencies up to above 1 MHz. In our experiments, the excitation coil is applied by a 4.3-V peak-to-peak voltage while the excitation frequency is changed to suitable the characteristics of the tested materials and it is determined by the experiments.

The main components of the experimental system include the output data processing system, data acquisition, and the x-y positioning system control of GMR sensor. As the output voltage of the GMR sensor is on the order of millivolt and hence vulnerable to wiring interference, the sensor output is amplified and filtered by the low noise pre-amplifier model SR560 from Stanford Research System. The pre-amplifier output is analyzed by the lock-in amplifier, model SR865A from Stanford Research Systems. The sensitivity of lock-in amplifier is set to be 100 mV. The dual-phase output is displayed on the front panel of the lock-in amplifier and available from the analog output ports. To read the output voltage of the sensor in real-time while scanning the sample surface, a data acquisition (DAQ) module USB-6216 from National Instruments was used to record the in-phase and quadrature eddy-current signals of GMR sensor all over the testing range on the sample surface. The data transmission and reading speed of the DAQ device is 400 kS/s. The data reading speed and acquisition rate are adjusted by the C# program to provide an accurate representation of the eddy-current signals in response to the scanning. To avoid interference induced by bending the signal transmission wires during scanning, the eddy-current probe is static while the object under test is mounted on a motor-controlled two-axis translation stage, model 08TMC-2 from Unice E-O Services Inc. The sample is mounted on a height and tilting adjustment mechanism to minimize the change in signal induced by the lift-off variation. The stepping motor controller is connected to a computer via a serial port. An in-house developed C# program is used to set the scanning range, velocity, and step size as well as to receive the eddy-current signal taken by the DAQ device.

## III. RESULTS AND DISCUSSIONS

### A. *Numerical model*

To evaluate performance as well as the underlying operation principle of the proposed probe, the eddy current density on the tested sample and the secondary magnetic field induced by the eddy current density are numerically analyzed using sofwares, MATLAB and ANSYS MAXWELL. In the numerical model, a rectangular excitation coil and underneath test sample with an arrangement of artificial cracks are used. The parameters and dimensions of the excitation coil used in the numerical model and the experiment are alike and are detailly described in Table I. A 40 mA sinusoidal current source is injected into the excitation coil with an excitation frequency of 40 kHz. For the test specimen, the simulated width and length of cracks are fixed 0.5 and 50 mm, respectively while the depth of them is varied by 0.1, 0.3, 0.5, 1.0, 1.5, and 1.8 mm.

To prove reliability of the finite element method, a numerical model is proposed to compare the results created by the ANSYS MAXWELL software and the results created by analytical expressions. In this model, when using a circular coil above a flawless semi-infinite conductor with conductivity of σ, the expression of the eddy current density can be determined by the following analytical expressions [24] using the MATLAB software. Then, the distribution of the eddy current density following the depth calculated from the sample surface is:

$$J(r,z) = j\frac{Ir_e}{\delta^2}\int_0^\infty J_1(\alpha r_e)J_1(\alpha r) \exp\left(-\left(\alpha L_1 - z\sqrt{\alpha^2 + j\left(2/\delta^2\right)}\right)\right)\times\frac{2\alpha}{\alpha+\sqrt{\alpha^2+j\left(2/\delta^2\right)}}d\alpha \quad (2)$$

Where $I$ is the excitation current, $r_e$ is the coil radius, $L_1$ is the liftoff distance between the coil bottom and the specimen surface, $r$ is distance between the calculated position of the eddy current density and the z-axis passing the coil center, $z \leq 0$ is the vertical coordinate calculated from the sample surface, $J_1(\alpha r_e)$ is Bessel first-order function of the first kind, $\delta = \sqrt{1/\pi f \mu\sigma}$ denotes skin depth.

And the distribution of the eddy current density at the surface is:

$$J(r_x,0) = -j\frac{\zeta}{\delta^2}\int_0^\infty J_1(\alpha r_e)J_1(\alpha r_x)\times\frac{2(e^{-\alpha L_1}-e^{-\alpha L_2})}{\alpha+\sqrt{\alpha^2+j(2/\delta^2)}}d\alpha \quad (3)$$

Where $r_x$ the horizontal coordinate with the origin determined by intersection between the z-axis passing the coil center and the sample surface, $\zeta$ (A/m) is the current density in the

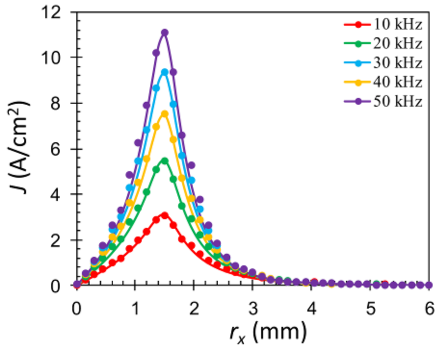


Fig. 7. Amplitude of the eddy current density along the x-axis on the spotless aluminum slab surface at frequencies of 10, 20, 30, and 40 kHz. Where the used excitation coil has the radius of 1.5 mm, the height of 0.05 mm, and the liftoff distance of $L_1$ = 0.2 mm, the surface current density of the excitation coil is $\zeta$ = 800 A/m.

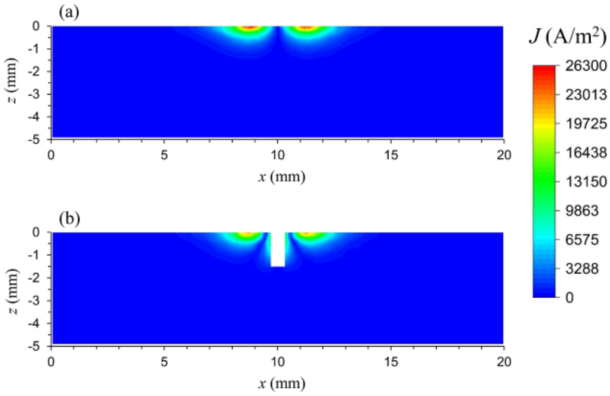


Fig. 8. The eddy current distribution following the depth of (a) spotless aluminum sample and (b) the flawed sample at the excitation ferquency of 40 kHz. The crack used in (b) has 0.5 mm width and 1.5 mm depth along the *y*-axis.

excitation coil, and $L_2$ - $L_1$ is the height of the excitation coil. The distribution of the simulated and calculated eddy-current density on the aluminum specimen surface along the x-axis with various frequencies of 10, 20, 30, and 40 kHz is presented in Fig. 7, where the continuous lines are the eddy current density calculated by analytical expressions Eq. (3) using MATLAB software, the solid circle symbols are the results obtained by the ANSYS software and the radius of the excitation coil is $r$ = 1.5 mm. It can be observed that the eddy current density is enhanced at the upper surface and its amplitude is larger when the higher excitation frequencies are applied. From the coil center and along the *x*-axis, the amplitude of the eddy current density increases gradually and reaches a peak near the coil radius then the amplitude decreases to zero as $x$ goes to infinity. It can be seen that, the obtained results from the analysis solution and the finite element method is a good discussion, thereby the ANSYS MAXWELL software is the useful software to evaluate the flaw detection in the conducting sample. The simulated eddy current distribution in the unflawed aluminum sample and the aluminum sample with the presence of a crack having a 1.5 mm depth and a 0.5 mm width is shown in Fig. 8. The eddy current density is most concentrated at positions around the radius of the excitation coil and it drops rapidly for locations away from the radius of the excitation coil. It can be found that the eddy current density on the spotless aluminum slab in Fig. 8(a)

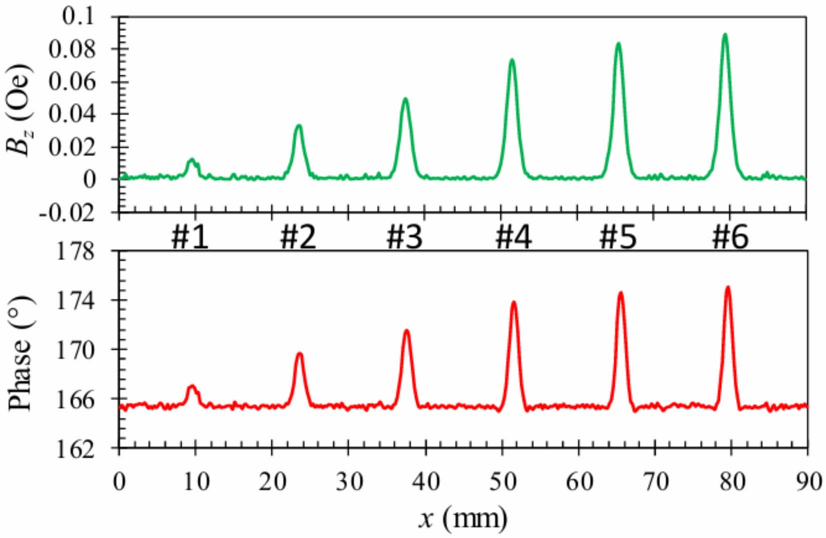


Fig. 9. The amplitude and phase signals of the $B_z$ component when scaning over cracks with different depths of 0.1, 0.3, 0.5, 1.0, 1.5, and 1.8 mm with the 40 kHz excitation frequency. The liftoff distance is 0.2 mm.

is higher than the eddy current density on the aluminum plate with the crack in Fig. 8(b) due to eddy current perturbations induced by crack. This leads to the variation of the secondary magnetic field induced by this eddy current with the presence of the crack. In our study, the novel design is used to detect the secondary magnetic field orthogonal to the sample surface and parallel to the excitation field, therefore the only $B_z$ component of the secondary magnetic field is collected and estimated in both the simulation and the experiment. In order to estimate the waveform of the output signals of the probe following the geometrical feature of simulated defects. The one-dimension (1D) scanning process was conducted by moving the excitation coil through surface slots on the aluminum plate with a step-by-step motion of 0.25 mm. Simulated cracks have the same width of 0.5 mm and the same length of 50 mm while the depth of cracks is varied by 0.1, 0.3, 0.5, 1.0, 1.5, and 1.8 mm, as defined in Fig. 4(b). The amplitude and phase angle field signals are collected. Fig. 9 shows the variation of $B_z$ magnetic field component for slots with different depths after subtracting the baseline magnetic field. It can be seen that the eddy currents are disturbed at positions having defects and the prominent peak values occur right cracks and the amplitude and phase signals are proportional to the depth of cracks. The simulated results show that the proposed probe is reliable to detect defects on the conducting material.

### B. *Frequency effect for surface and subsurface defect detection*

One of the most important goals in eddy current testing is to find out characteristics of the defect such as the geometrical dimensions, position as well as its orientation and depth, etc. Thereby, to achieve the best performance and best defect characterization of the fabricated probe for detecting surface and subsurface defects in the specific cases, it is essential that the probe is operated in the optimal frequency range so that the defect information is clearly observed and can be reconstructed. When the high excitation frequency is used, the signals from the field magnetic sensor increase due to the enhancement of the eddy current density. However, the deeper defect inspection is limited by the skin depth, which is lower at higher frequencies, the obtained signals from surface or subsurface defects can not be detected. For detecting deep or

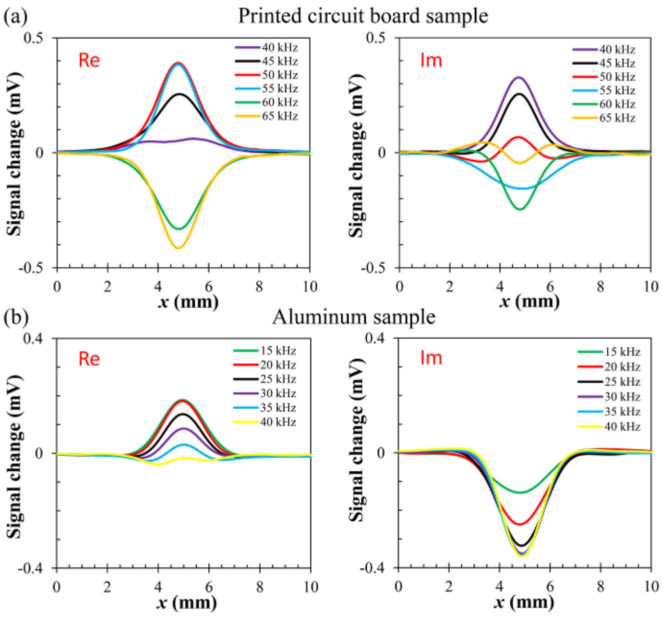


Fig. 10. Waveform and signal intensity change of the in-phase (*Re*) and quadrature (*Im*) components when the probe scans over a crack at different frequencies. (a) For PCB sample with metal loss of a 0.8 mm wide slot, (b) For aluminum sample with a 0.5 mm wide and 1.5 mm deep crack defect buried at $h$ = 0.095 mm.

subsurface defects, the low inspection frequency should be used to enhance the skin depth. However, if the excitation frequency is too low, the output signal of the field magnetic sensor decreases and may be affected by the system noise floor, and thus limiting the performance of the probe. To find the optimal excitation frequency, the in-phase (*Re*) and quadrature (*Im*) output signals are recorded on a crack buried at different depths from the sample surface in a wide range of frequencies. For the PCB sample, a 0.8 mm wide and 15 mm long surface crack is tested with frequencies from 20 kHz to 75 kHz with steps of 5 kHz. For the aluminum sample, a 0.5 mm wide and 1.5 mm deep crack buried at different depths of $h$ = 0, 0.095, and 0.285 mm is inspected in the frequency range between 5 kHz and 50 kHz in steps of 5 kHz. The 1D-scanned data on PCB and aluminum samples is shown in Fig. 10(a) and (b), respectively. It can be found that the waveform of the output signals after subtracting the baseline voltage at corresponding frequencies is changed, the maximum value occurs near the crack on both samples. For the PCB specimen, the *Re* and *Im* components presented a significant change in the signal intensity. At the 55 kHz excitation frequency, the *Im* component is changed in the opposite direction compared with the *Re* component while the trend of the *Im* signal change at the remaining frequencies of 40, 45, 50, 60, and 65 kHz is in the same direction compared with the *Re* signal. For the aluminum sample with a 1.5 mm deep crack located at a 0.095 mm depth beneath the sample surface, the change of the *Re* and *Im* signals at all frequencies of 15, 20, 25, 30, 35, and 40 kHz is in the opposite direction and the *Im* signal is large compared with the *Re* signal at all frequencies. The optimal excitation frequency is affected by many factors, consisting of the skin depth, conductivity and permeability of the material, and shape and buried depth of defects. Fig. 11 shows the amplitude change of the aluminum and PCB samples at different excitation

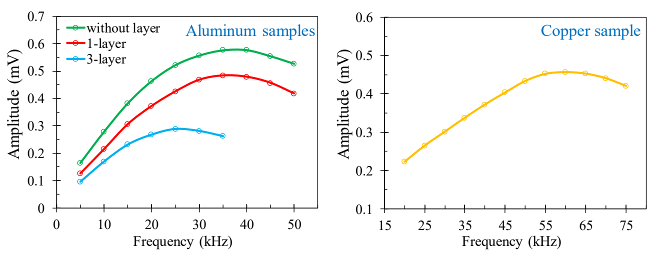


Fig. 11. The resultant amplitude of the EC signals at different frequencies. (a) For aluminum samples with a 0.5-mm wide and 1.5-mm deep crack buried at $h$ = 0, 0.095, and 0.285 mm, respectively. For printed circuit board with a 0.8-mm wide and 15-mm long surface crack.

frequencies. It is observed that when the excitation fryquency increases the amplitude increases initially and peaks at the optimal excitation frequency, and gradually decreases afterwards. This variation trend is caused by the skin depth effect. When increasing the excitation frequency, the amplitude of the EC signals gradually increases since the induced EC density tends to be concentrated at the upper surface of the sample. However, at the higher excitation frequencies, the EC density is strongly reduced with depth calculated from the top surface and the amplitude of the EC signals is influenced by the amplitude attenuation more than the small linear amplitude augmentation of the EC density at the upper surface of the sample so the amplitude decreases immediately after the optimal excitation frequency. The experimental results show that the optimal excitation frequency of the aluminum samples for cracks buried at $h$ = 0, 0.095, 0.285 mm is 40, 35, and 25 kHz, respectively and the corresponding skin depth at these frequencies is 0.41, 0.44, and 0.52 mm. For the PCB sample, the optimal frequency is found 60 kHz and the skin depth is 0.27 mm which is larger the thickness of 0.05 mm of the copper layer.

C. *Surface and subsurface flaws on aluminum plate*

To assess the detection capability of the probe and investigate the effect of the shape and position of flaws on the tested sample. Experimental studies with 1D-scanned process (B-scan) are performed on aluminum samples, as described in Fig. 4 and surface and subsurface defects are inspected at the optimal excitation frequency of 40, 35, and 25 kHz for cracks buried at $h$ = 0, 0.095, and 0.285 mm under the top surface, respectively. The amplitude and phase output signals of the eddy-current probe are recorded to analyze when the aluminum specimen moves under the probe with step size of 0.125 mm and the liff-off distance between the bottom of the probe and the specimen surface under test is 0.2 mm. By this way, the signal at the central region of each crack was collected. Fig. 12, 13, and 14 show the relationship between the defect field with flaws #1 to #6 and the output signal of the EC probe for detecting surface and subsurface cracks buried at $h$ = 0, 0.095, and 0.285 mm, respectively. It can be seen that all of the antificial cracks on the tested specimen are detected by the proposed probe; the amplitude and the corresponding phase angle of the output signals are significantly changed when the probe scans cross the cracks having different depths of 0.1, 0.3, 0.5, 1.0, 1.5, and 1.8 mm. The position of the cracks is denoted by the peak or valley values in the amplitude and phase signals which appear right at the center of the cracks. The magnitude of

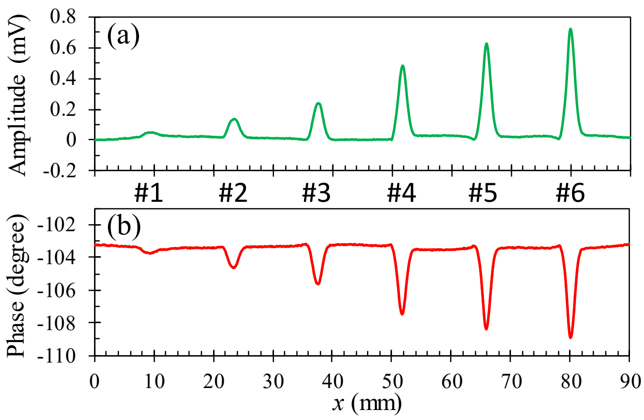


Fig. 12. Inspection of surface cracks ($h$ = 0 mm) at the optimal excitation frequency of 40 kHz. (a) Amplitude variation. (b) Phase angle variation.

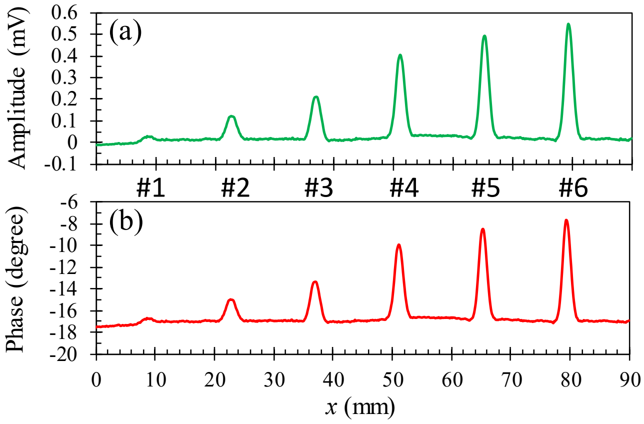


Fig. 13. Inspection of subsurface cracks ($h$ = 0.095 mm) at the optimal excitation frequency of 35 kHz. (a) Amplitude variation. (b) Phase angle variation.

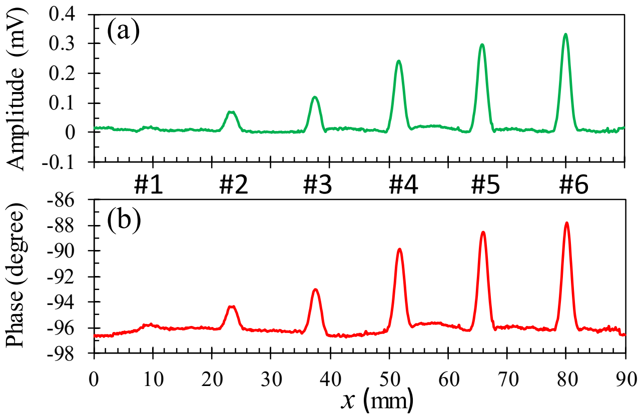


Fig. 14. Inspection of subsurface cracks ($h$ = 0.285 mm) at the optimal excitation frequency of 25 kHz. (a) Amplitude variation. (b) Phase angle variation.

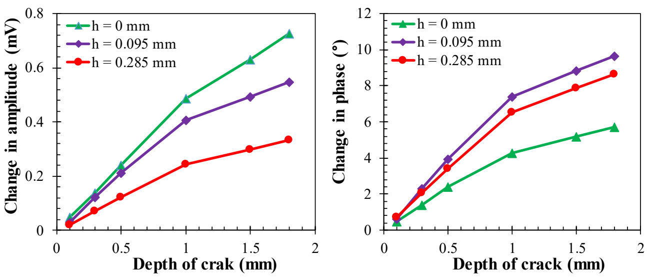


Fig. 15. Relation of the amplitude and phase signals to crack depth for flaws buried at $h$ = 0, 0.095, and 0.285 mm.

the peak or valley values depends on the crack depth, when the depth of cracks increases, the peak or valley values of the EC signals also rises, as shown in Fig. 12, 13, and 14. Although all cracks of different depths of 0.1, 0.3, 0.5, 1.0, 1.5, and 1.8 mm at $h = 0$, 0.095, and 0.285 mm are detected by the EC probe, especially the 0.1-mm deep crack buried up to $h = 0.285$ mm is clearly observed in both the amplitude and phase signals. However, the obtained EC signals are significantly noised for subsurface flaws with an increasing buried depth, as shown in Fig. 13 and 14. To consider the sensitivity for detecting the cracks of different depths at $h = 0$, 0.095, and 0.285 mm below the top surface, the largest change in amplitude and phase values when the probe scans through the crack region are computed. Fig. 15 shows the respective average sensitivity for detecting the cracks of different depths buried at $h = 0$, 0.095, and 0.285 mm. The results present the peak or valley values as a function of the crack depth. In the change of the amplitude signal, the detection of the surface crack has the highest sensitivity and the sensitivity gradually decreases as the increasing burial as shown in Fig. 15(a). While the phase sensitivity is larger for detecting buried cracks in comparison with surface cracks, as shown in Fig. 15(b). The results presented good agreement between simulated signals and experimental signals from the proposed probe.

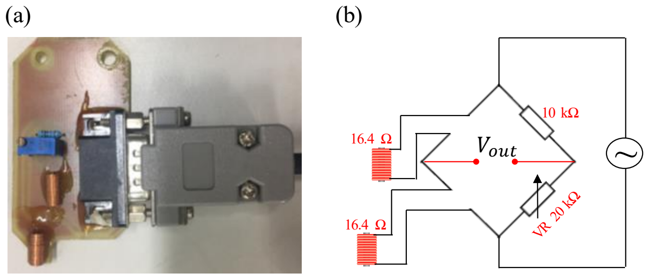


Fig. 16. The coil-based probe: (a) the photograph and (b) circuit diagram of the coil probe.

*D. Flaw inspection on the printed circuit board*

To evaluate the performance of the proposed probe with high spatial resolution, imaging the shape of two-dimensional (2D) defects is conducted on a PCB sample with artificial defects having the complex shape as described in Fig. 5. The defect inspection with 2D image is realized at the excitation frequencies of 55 and 60 kHz. Besides, the performance of the proposed probe is compared with that of the coil-based probe having a 4.0-mm diameter of the sensing coil. In the coil probe, two coils (a sensing coil and a reference coil) and two resistors are formed to the bridge output as shown in

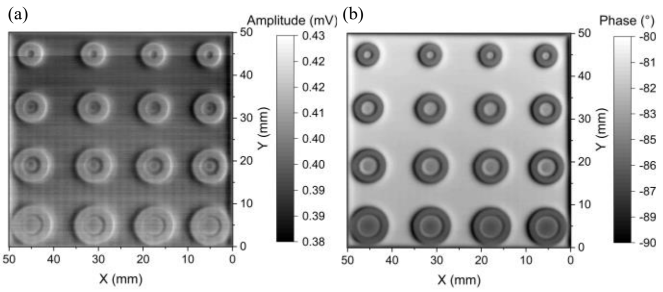


Fig. 17. C-scan image with the excitation frequency of 55 kHz: (a) The amplitude image, and (b) the phase image.

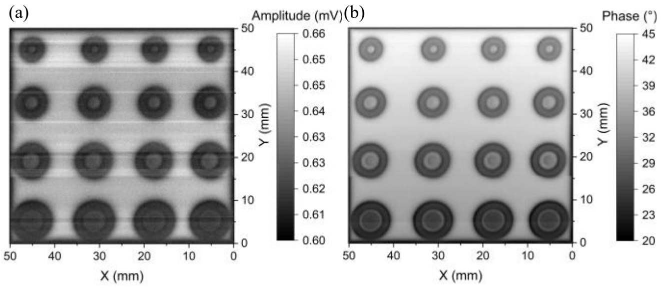


Fig. 18. C-scan image at the excitation frequency of 60 kHz: (a) The amplitude image, and (b) the phase image.

Fig. 16 where one of two resistors is a variable resistor of 20 kΩ to adjust the output voltage. For the performance of both probes, the tested sample is moved with the step size of 0.125 mm while the probe is static to avoid interference caused by the connected wires. The amplitude and phase signals are saved to form the 2-D image and extract the characteristics of defects on the tested sample. For the proposed probe, Fig. 17 and 18 show the 2D eddy-current images collected from the amplitude and phase signals at excitation frequencies of 55 and 60 kHz, respectively, when the probe scans over the sample surface.

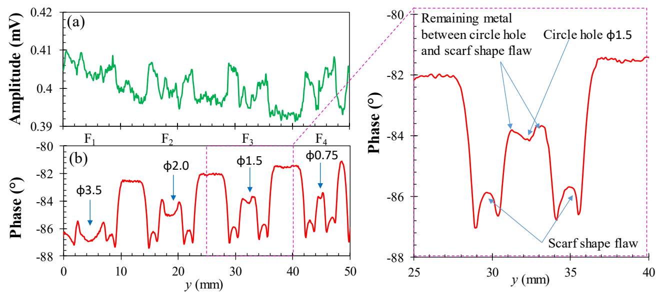


Fig. 19. The (a) amplitude and (b) phase signals extracted from the line at x = 5 mm along the center of flaws $F_1$, $F_2$, $F_3$, and $F_4$.

It can be seen that the shape and dimension of the machined flaw types are clearly observed in the phase figures while the amplitude images are significantly blurred and the inside circle holes of flaws $F_1$, $F_2$, $F_3$, and $F_4$ can not be distinguished in the amplitude images. The amplitude and phase values extracted from the line $x = 5$ mm along the center of the flaws $F_1$, $F_2$, $F_3$, and $F_4$ are shown in Fig 19.

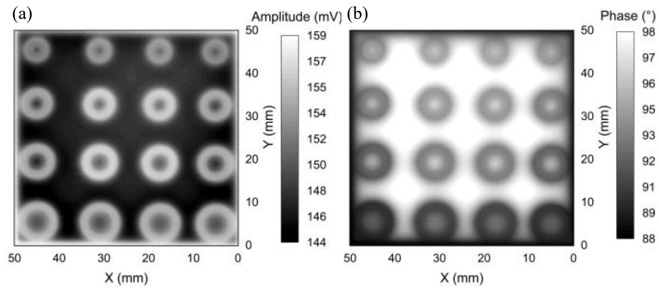


Fig. 20. C-scan image at the excitation frequency of 55 kHz of the coil probe: (a) The amplitude image, and (b) the phase image.

The signals are changed when scanning over flaws having different shapes and dimensions and the characteristic signal of a flaw including an inside circle hole, a scarf shape flaw, and the metallic part between them are shown in the inset of Fig. 19. It indicates that all of the flaws on the tested sample are detected even if the inside circle hole of flaw $F_1$ having a small diameter of 0.75 mm is also detected by the proposed probe as shown in Fig. 19(b). For the coil probe, the 2D eddy-current images of the amplitude and phase angle obtained by the probe are shown in Fig. 20. It is found that the features of the defect are more clearly observed in the amplitude image in comparison with the phase image. However, the metal part between the inside circle hole and the scarf shape defect in flaws $F_1$, $F_2$, $F_3$, and $F_4$ can not be distinguished and the shape of minor defects is not specifically reflected in amplitude and phase images. By comparing Fig. 17 and 18 with Fig. 20, it can be observed that the performance of the proposed probe is more superior with more sensitivity and higher spatial resolution in the EC images compared with the coil probe having similar size even if the coil-based probe having a 1-mm diameter is used.

## IV. CONCLUSION

A novel design of the miniature half-bridge GMR-based eddy current probe allows the location and estimation of geometrical features of flaws on the tested sample with high spatial resolution and high sensitivity. It is able to detect small defects with the geometrical size less than 1 mm on the sample surface and subsurface. The experimental results presented that the proposed probe can detect a subsurface crack with a minimum depth of 0.1 mm buried up to 0.285 mm from the top surface on the aluminum plate. For the surface flaws on the PCB sample, the 2D eddy-current images obtained by the assembled probe can determine geometrical size and locate flaws having the complex shape. Especially, the inside small circle hole of flaw $F_1$ which has a 0.75-mm diameter is also detected by the developed probe. Besides, with the characteristics of small size, high spatial resolution and high sensitivity the performance of the proposed probe gives better results in comparison with the performance of the coil-based probe having the similar size. Therefore, the miniature GMR-based probe is useful for detecting minor surface and subsurface defects such as mechanical cracks, corrosion, and short circuits in printed circuit boards.


## ACKNOWLEDGMENT

We thank the National Center for High-performance Computing of National Applied Research Laboratories in Taiwan for providing computational resources.


## REFERENCES


[1] S. K. Burke, "Eddy-current inversion in the thin-skin limit: Determination of depth and opening for a long crack," *Journal of Applied Physics*, vol. 76, no. 5, pp. 3072-3080, 1994.

[2] S. K. Burke and R. J. Ditchburn, "Mutual impedance of planar eddycurrent driver–pickup spiral coils," *Res. Nondestruct. Eval*., vol. 19, no. 1, pp. 1–19, Jan. 2008.

[3] O. Bíró, "Edge element formulations of eddy current problems," *Comput. Methods Appl. Mech. Eng*., vol. 169, nos. 3–4, pp. 391–405, Feb. 1999.

[4] T. Theodoulidis, N. Poulakis, and A. Dragogias, "Rapid computation of eddy current signals from narrow cracks," *NDT E Int*., vol. 43, no. 1, pp. 13–19, Jan. 2010.

[5] Y. Xu, Y. Yang, and Y. Wu, "Eddy Current Testing of Metal Cracks Using Spin Hall Magnetoresistance Sensor and Machine Learning," *IEEE Sensors Journal,* vol. 20, no. 18, pp. 10502-10510, 2020.

[6] J. T. Jeng, S. Y. Yang, H. E. Horng and H. C. Yang, "Detection of deep flaws by using a HTS-SQUID in unshielded environment," in *IEEE Transactions on Applied Superconductivity*, vol. 11, no. 1, pp. 1295-1298, 2001.

[7] J. T. Jeng, H. E. Horng, H. C. Yang, J. C. Chen, and J. H. Chen, "Simulation of the magnetic field due to defects and verification using high-Tc SQUID," *Phys. C, Supercond*., vol. 367, pp. 298–302, Feb. 2002.

[8] C. H. Smith, R. W. Schneider, T. Dogaru, & S. T. Smith, "Eddy-Current Testing with GMR Magnetic Sensor Arrays", *In AIP Conference Proceedings*, Vol. 700, No. 1, pp. 406-413, American Institute of Physics (2004, February).

[9] O. Postolache, A. L. Ribeiro, and H. G. Ramos, "GMR array uniform eddy current probe for defect detection in conductive specimens", *Measurement*, 46(10), 4369-4378 (2013).

[10] G. Lin, D. Makarov, & O. G. Schmidt, "Magnetic sensing platform technologies for biomedical applications", *Lab on a Chip*, 17(11), 1884-1912 (2017).

[11] V. S. Luong, Y.-H. Su, C.-C. Lu, J.-T. Jeng, J.-H. Hsu, M.-H. Liao, J.-C. Wu, M.-H. Lai, C.-R. Chang, "Planarization, Fabrication and Characterization of Three-dimensional Magnetic Field Sensors", *IEEE Transactions on Nanotechnology*, Vol. 17, no. 1, pp.11 - 25 (2018).

[12] O. Karpenko, A. Efremov, C. Ye, and L. Udpa, "Multi-frequency fusion algorithm for detection of defects under fasteners with EC-GMR probe data," *NDT & E International,* vol. 110, 2020.

[13] H. Ehlers, M. Pelkner, and R. Thewes, "Heterodyne Eddy Current Testing Using Magnetoresistive Sensors for Additive Manufacturing Purposes," *IEEE Sensors Journal,* vol. 20, no. 11, pp. 5793-5800, 2020.

[14] C. Ye, Y. Huang, L. Udpa, and S. S. Udpa, "Differential Sensor Measurement With Rotating Current Excitation for Evaluating Multilayer Structures," *IEEE Sensors Journal,* vol. 16, no. 3, pp. 782-789, 2016.

[15] S. B, A. V, M. C.K, and R. B.P.C, "Enhanced detection of deep seated flaws in 316 stainless steel plates using integrated EC-GMR sensor," *Sensors and Actuators A: Physical,* vol. 275, pp. 44-50, 2018.

[16] K. Chomsuwan, S. Yamada, and M. Iwahara, "Bare PCB Inspection System With SV-GMR Sensor Eddy-Current Testing Probe," *IEEE Sensors Journal,* vol. 7, no. 5, pp. 890-896, 2007.

[17] D. J. Pasadas, A. L. Ribeiro, T. Rocha, and H. G. Ramos, "2D surface defect images applying Tikhonov regularized inversion and ECT," *NDT & E International,* vol. 80, pp. 48-57, 2016.

[18] T. Dogaru and S. T. Smith, "Giant magnetoresistance-based eddy-current sensor", IEEE Transactions on Magnetics, vol. 37, no. 5, pp. 3831-3838, 2001.

[19] N. O. Romero-Arismendi, J. A. Pérez-Benítez, E. Ramírez-Pacheco, and J. H. Espina-Hernández, "Design method for a GMR-based eddy current sensor with optimal sensitivity," Sensors and Actuators A: Physical, vol. 314, 2020.

[20] B. Helifa, A. Oulhadj, A. Benbelghit, I. K. Lefkaier, F. Boubenider, and D. Boutassouna, "Detection and measurement of surface cracks in ferromagnetic materials using eddy current testing," NDT & E Int., vol. 39, no. 5, pp. 384–390, 2006.

[21] M. Lu, X. Meng, R. Huang, A. Peyton, and W. Yin, "Analysis of Tilt Effect on Notch Depth Profiling Using Thin-Skin Regime of Driver-Pickup Eddy-Current Sensor," *Sensors (Basel),* vol. 21, no. 16, Aug 17 2021.

[22] M. Fan, Q. Wang, B. Cao, B. Ye, A. I. Sunny, and G. Tian, "Frequency Optimization for Enhancement of Surface Defect Classification Using the Eddy Current Technique," *Sensors (Basel),* vol. 16, no. 5, May 7 2016.

[23] E. S. Boltz and T. C. Tiernan, "New electromagnetic sensors for detection of subsurface cracking and corrosion," Rev. Prog. Quant. Non-Destruct.Eval., vol. 17, pp. 1033–1038, 1998.
[24] J. R. Claycomb, N. Tralshawala, H. M. Cho, M. Boyd, Z. Zou, X. W. Xu, J. H. Miller Jr, "Simulation and design of a superconducting eddy current probe for nondestructive testing", Review of scientific instruments, vol. 69, no.2, 499-506, 1998.